Experimental Section

Chemicals. Iron(III) nitrate nonahydrate ($Fe(NO_3)_3 \cdot 9H_2O$, 99.99%), gold(III) chloride trihydrate ($HAuCl_4 \cdot 3H_2O$, 99.99%), glycerol ($C_3H_8O_3$, 99.5%), 2-propanol (C_3H_8O, 99.5%), sodium hydroxide (NaOH, 98%), and ethanol (99.5%) were purchased from Sigma-Aldrich Japan. All the chemicals were used without further purification.

Synthesis of mesoporous γ-Fe_2O_3 nanoflakes. In a typical procedure, 0.202 g of $Fe(NO_3)_3 \cdot 9H_2O$ was dissolved in 40 mL of 2-propanol under magnetic stirring. Following this, 10 mL of glycerol was slowly added into this solution and stirred until homogeneously mixed. The resulting mixture was subsequently placed into stainless steel-lined Teflon autoclave and heated at 180 ºC for 16 h and cooled to room temperature naturally. Next, the product was thoroughly washed with absolute ethanol for several times, before being dried in an electric oven at 60 ºC. The dried powder was then calcined under air atmosphere at 350 ºC for 2 h, with a heating rate of 1 °C/min. For comparison, the same dried powder was also calcined at 250 ºC, 300 ºC, and 400 ºC for 2 h under similar heating rate. The samples calcined at 250 ºC, 300 ºC, 350 ºC, and 400 ºC are labeled as Fe-MNF-250, Fe-MNF-300, Fe-MNF-350, and Fe-MNF-400, respectively.

Deposition of Au nanoparticles (Au NPs) into mesoporous γ-Fe_2O_3 nanoflakes. The loading of Au NPs onto the mesoporous γ-Fe_2O_3 nanoflakes was achieved via a sequential deposition-precipitation (DP) process. In a typical process, 100 mL of 1000 ppm $HAuCl_4$ solution was initially prepared. This solution was then heated to 70 °C in a water bath and the pH was adjusted to 7 through the addition of NaOH solution. After being cooled to room temperature, 50 mg of the precursor nanoflakes was added into this solution and the resulting mixture solution was subsequently stirred at 70 °C for 1 h. The product was collected via filtration and washed with distilled water for several times and finally, dried under vacuum. Lastly, the dried powder was calcined in air for 2 h at various temperatures, including 250 °C, 300 °C, 350 °C and 400 °C with a fixed heating rate at 5 ºC /min and the obtained products are labeled as Au/Fe-MNF-250, Au/Fe-MNF-300, Au/Fe-MNF-350, and Au/Fe-MNF-400, respectively.

Catalytic test for CO oxidation. The catalytic tests for CO oxidation were conducted using a continuous-flow fixed-bed reactor system. In a typical procedure, 4 mg of the catalyst (40 mg for the Au-loaded commercial Fe_2O_3) is placed into a U-shape quartz reactor (50 mm x 1 mm) and heated to 250 °C under 0.1 L min^{-1} of air flow for 30 min. Following this, 1000 ppm of CO in air was flowed into the reactor at a predetermined flow rate and the reaction was conducted at 25 °C and a humidity level of 60%. The CO conversion was calculated from the change in the CO concentration, as calculated using the following equation:

$$\text{CO conversion (\%)} = \frac{[CO]in - [CO]out}{[CO]in} \times 100\% \qquad (1)$$

To determine the influence of flow rate on the CO conversion, the CO gas flow rate was varied from 0.1 L min^{-1}

to 5 L min^{-1}.

Characterization. The morphological observations of the as-prepared samples were conducted using scanning electron microscope (SEM) (Hitachi SU-8000) operated at an accelerating voltage of 5 kV and transmission electron microscope (TEM) (JEOL JEM-2100F) operated at an accelerating voltage of 200 kV. The phase composition and crystal structure of the samples were analyzed using X-ray diffraction (Shimadzu XRD-7000) with Cu-Kα (1.54 Å). X-ray photoelectron spectroscopy (XPS) measurements were performed with a PHI Quantera SXM instrument. All binding energies were calibrated by referencing to the C1s line (285.0 eV). Fourier transform infrared (FTIR) spectra were collected on a Thermo scientific Nicolet 4700 spectrometer. Thermogravimetric analysis (TGA) was carried out using a Hitachi HT-Seiko Instrument Exter 6300 TG from room temperature to 800 °C under air atmosphere with a heating rate of 10 °C/min. Inductively coupled plasma optical emission spectrometry (ICP-OES) measurement was carried out using a Hitachi model SPS3520UV-DD. Nitrogen (N_2) adsorption-desorption measurements were performed using a Belsorp-mini II Sorption System at 77 K. The specific surface areas and pore size distribution of the samples were determined using the multipoint Brunauer-Emmett-Teller (BET) and Barrett-Joyner-Halenda (BJH) methods, respectively. Prior to the BET measurements, each sample was degassed at 150 °C for 16 h.

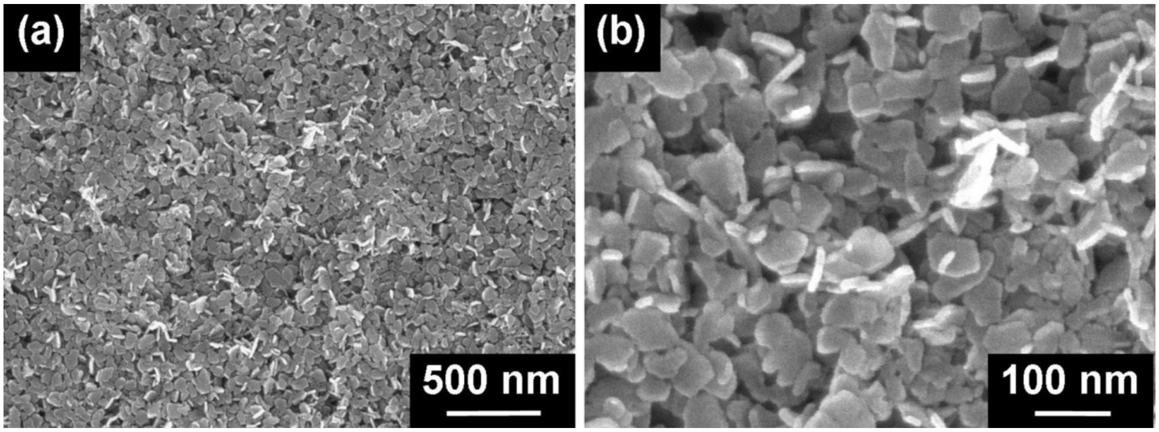

Fig. S1. SEM images of the product obtained from the solvothermal reaction between ferric nitrate nonahydrate and glycerol (10 mL) at 180 °C for 16 h.

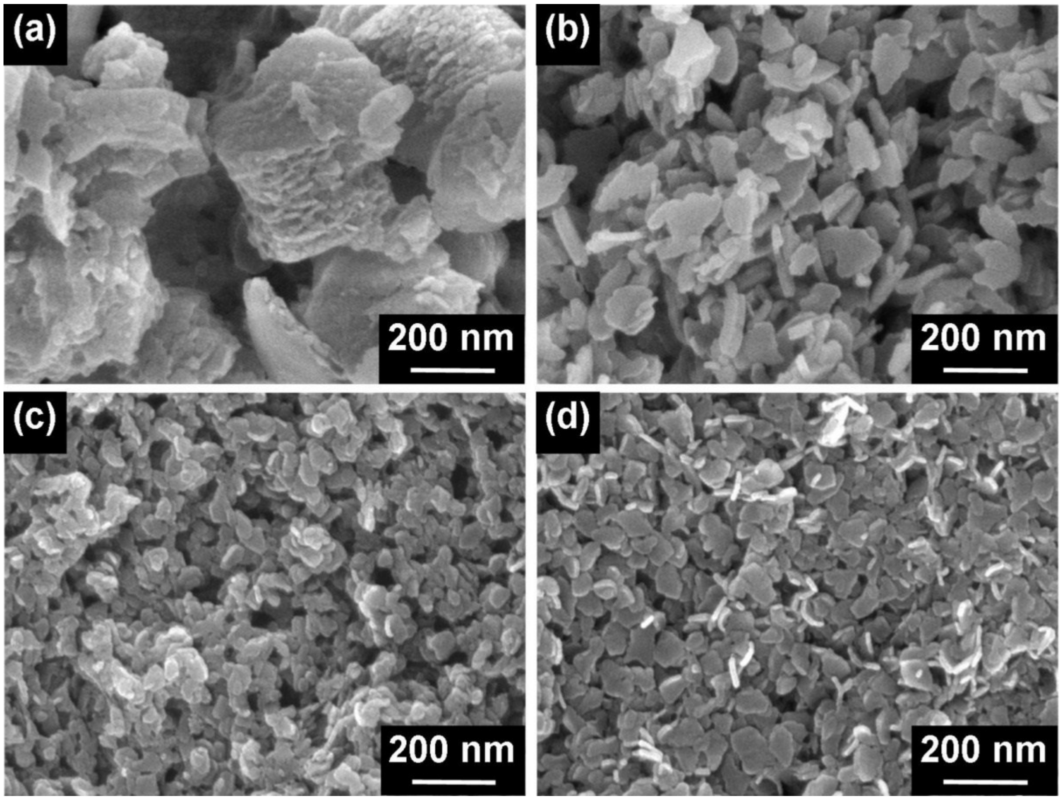

Fig. S2. SEM images of the products obtained using (a) 2 mL, (b) 4 mL, (c) 8 mL, and (d) 10 mL of glycerol, respectively at 180 °C for 16 h under solvothermal conditions.

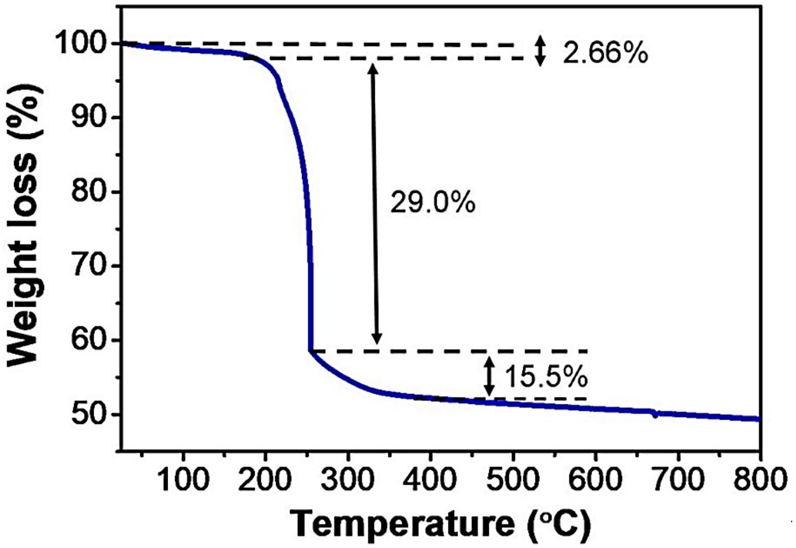

Fig. S3. Thermogravimetric analysis (TGA) of the iron glycerate nanoflakes from room temperature to 800 ºC under air atmosphere with a heating rate of 10 ºC/min.

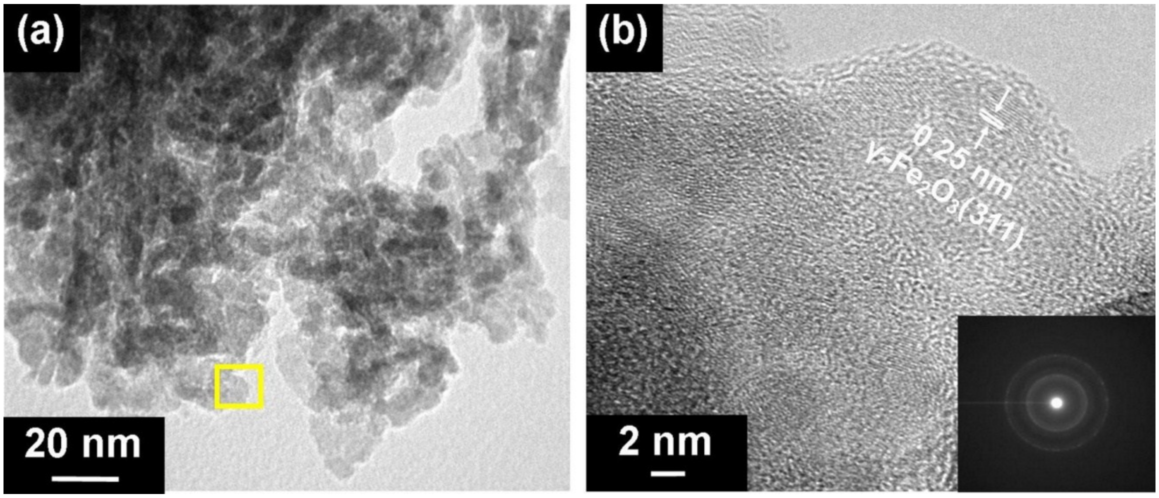

Fig. S4. (a) TEM and (b) HRTEM images of mesoporous γ-Fe_2O_3 nanoflakes obtained from the calcination of iron glycerate nanoflakes in air at 350 ºC (Fe-MNF-350).

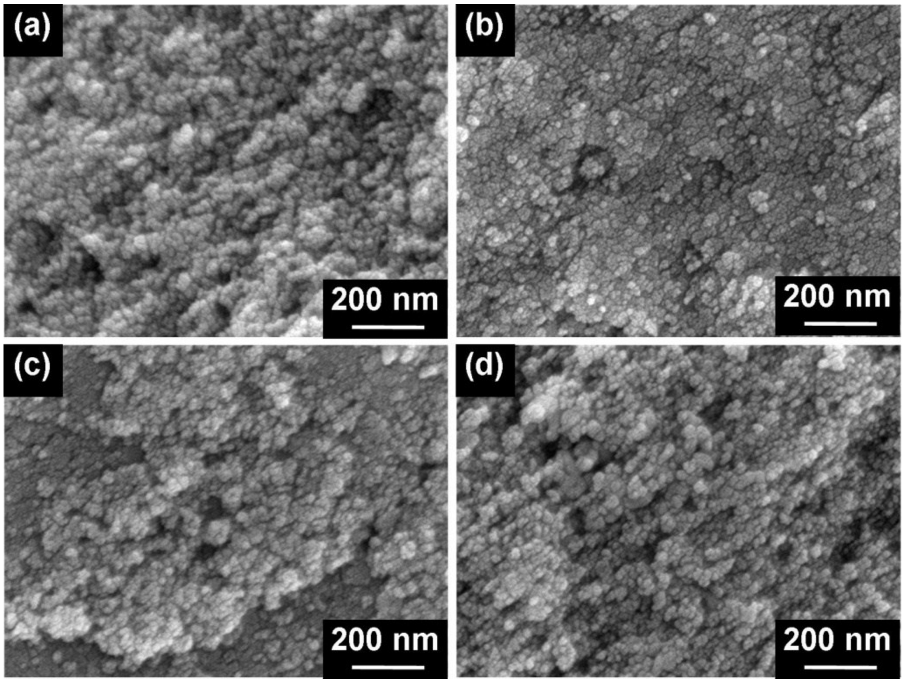

Fig. S5. SEM images of the Au-loaded mesoporous iron oxide nanoflakes obtained at calcination temperatures of (a) 250 ºC (Au/Fe-MNF-250), (b) 300 ºC (Au/Fe-MNF-300), (c) 350 ºC (Au/Fe-MNF-350), and (d) 400 ºC (Au/Fe-MNF-400).

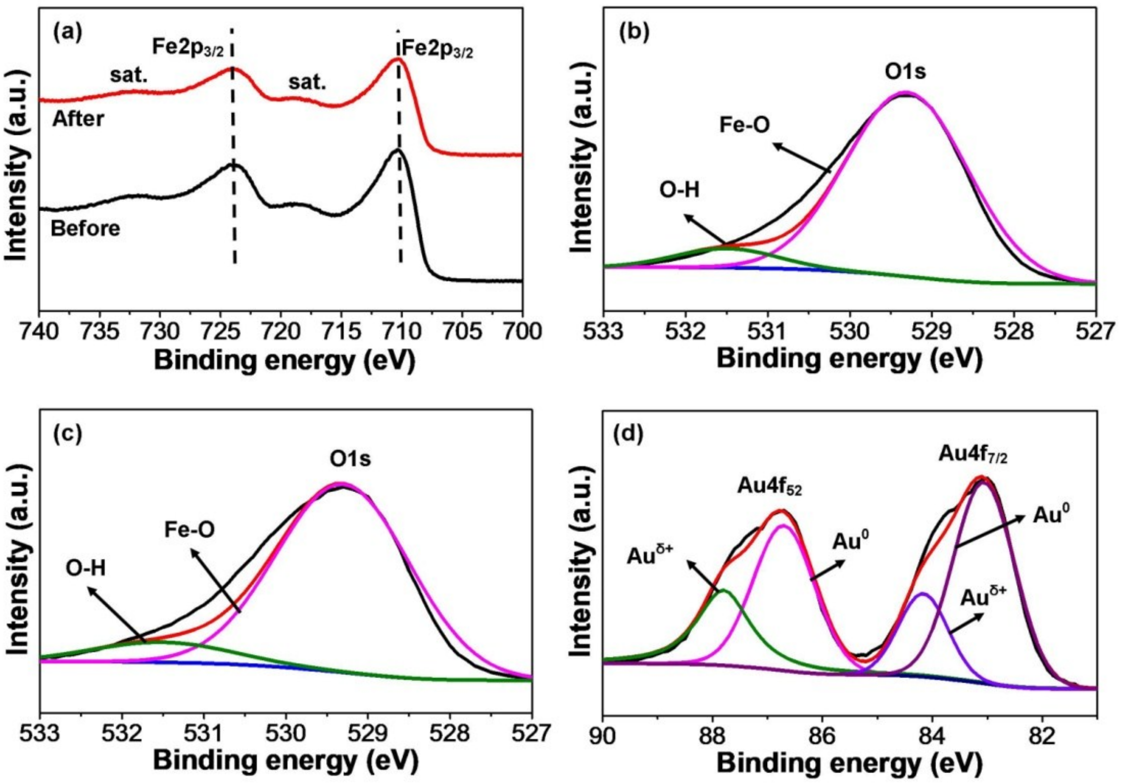

Fig. S6. (a) Comparison of high resolution Fe2p XPS spectra of Fe-MNF-350 and Au/Fe-MNF-350. High resolution XPS spectra of O1s for Fe-MNF-350 (b) and Au/Fe-MNF-350 (c). (d) The high resolution Au4f XPS spectrum of Au/Fe-MNF-350.

Notes for Fig. S6: The high resolution Fe2p peaks of Fe-MNF-350 appearing at 723.9 eV and 710.3 eV can be indexed to Fe2p$_{3/2}$ and Fe2p$_{1/2}$ peaks, respectively, with the binding energy difference being 13.6 eV (**Fig. S6a**). Furthermore, the presence of satellite peaks at 719.2 eV and 723.6 eV are characteristics of Fe^{3+}.[1] After the Au loading, the Fe2p$_{3/2}$ peak is slightly shifted to 724.0 eV, which may be attributed to the Au NPs/γ-Fe$_2$O$_3$ electronic interaction.[2] The deconvoluted O1s spectrum of Fe-MNF-350 displays two peaks at 529.3 eV and 531.5 eV, corresponding to Fe-O and adsorbed water, respectively and these peaks remain more or less similar after the modification with Au NPs (**Fig. S6b-c**). The deconvoluted Au4f peaks reveal the presence of Au^0 and Au$^{+\delta}$, as seen in **Fig. S6d**.[3]

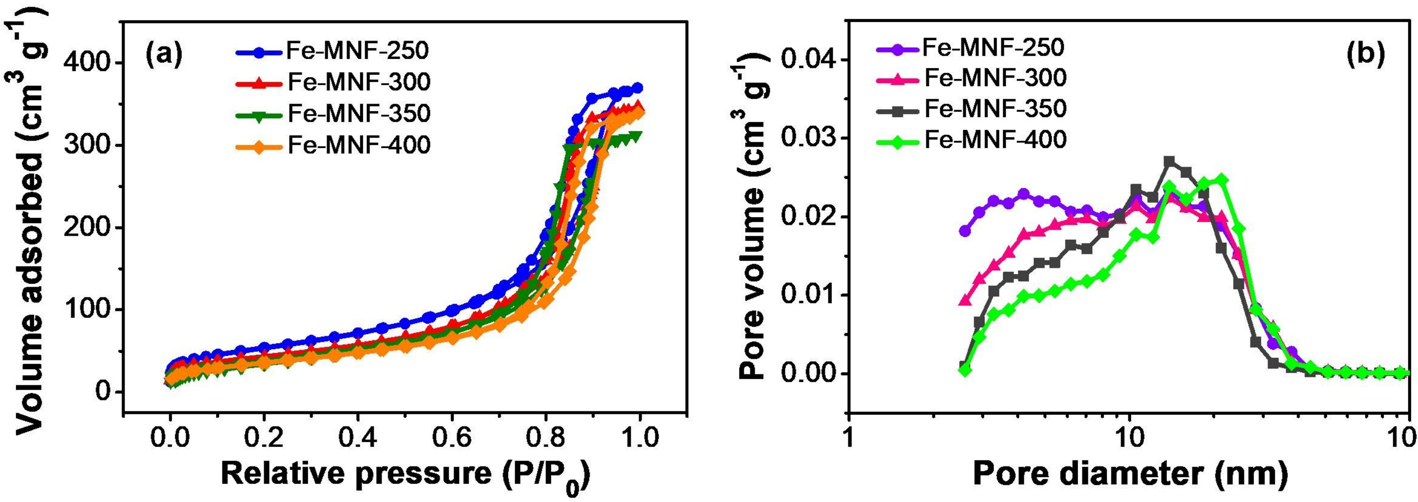

Fig. S7 Nitrogen (N_2) adsorption-desorption isotherms and pore size distribution (PSD) curves of the mesoporous iron oxide nanoflakes obtained at different calcination temperatures.

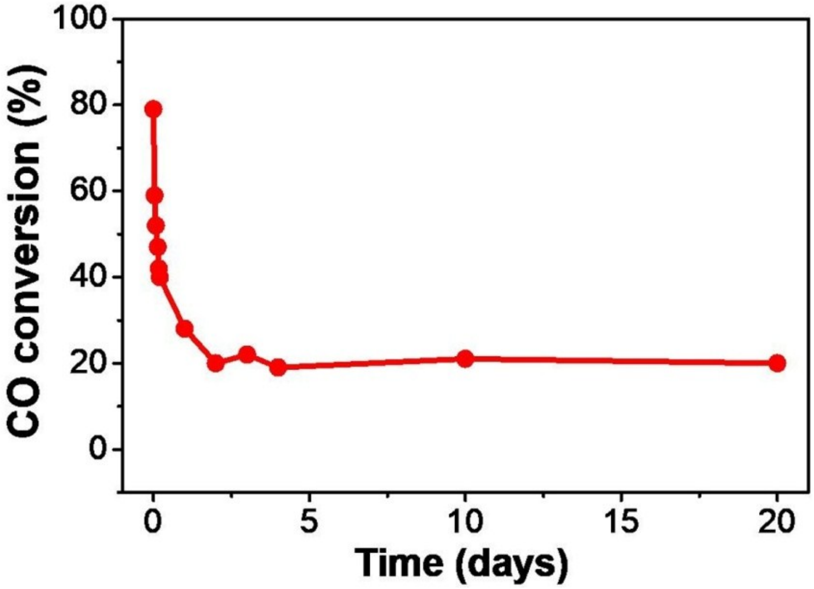

Fig. S8. Recylability test results of the Au/Fe-MNF-350 for CO oxidation for 20 days (amount of catalyst = 4 mg, CO flow rate = 1 L min^{-1}, temperature = 25 ºC, humidity = 60%)

Notes for Fig. S8: The recyclability test of the Au/Fe-MNF-350 catalyst for CO oxidation was evaluated at 25 ºC and a humidity level of 60% under CO flow rate of 1 L min^{-1} for 20 days. The results reveal that the Au/Fe-MNF-350 catalyst shows a decrease of 37% in activity after 5 h of reaction, before eventually reaches a stable CO conversion of around 20% starting from day 2 to day 20.

Table S1. Textural characteristics of the mesoporous iron oxide nanoflakes obtained at different calcination temperatures

Sample	**Calcination temperature (ºC)**	**Main cystal phase**	**Specific surface area ($m^2\ g^{-1}$)**	**Pore volume ($cm^3\ g^{-1}$)**	**Mean pore diameter (nm)**
Fe-MNF-250	250	γ-Fe_2O_3	193	0.57	11.8
Fe-MNF-300	300	γ-Fe_2O_3	153	0.53	13.8
Fe-MNF-350	350	γ-Fe_2O_3	140	0.48	13.9
Fe-MNF-400	400	α-Fe_2O_3	130	0.52	16.0

Table S2. Specific activities of the Au-loaded mesoporous iron oxide nanoflakes obtained at different calcination temperatures for CO oxidation and comparison with previously reported Au/Fe_xO_y catalysts.

Sample	**Catalyst amount (g)**	**Au loading (wt%)**	**Specific activity ($mol_{CO}\ g_{Au}^{-1}\ h^{-1}$)#**	**Ref.**
Au/Fe-MNF-250	0.004	15.5	4.93	This work
Au/Fe-MNF-300	0.004	13.1	4.38	This work
Au/Fe-MNF-350	0.004	12.9	8.41	This work
Au/Fe-MNF-400	0.004	9.80	7.67	This work
Au/comm-Fe_2O_3	0.04	0.81	1.46	This work
Au/α-Fe_2O_3	0.5	0.50	0.12	[4]
Au/γ-Fe_2O_3	n/a	0.95	3.31	[5]
Au/α-Fe_2O_3	0.05	2.90	2.12	[6]
Au/α-Fe_2O_3-C	0.05	2.90	0.40	[6]
Au/Fe_2O_3-WGC	0.10	4.40	0.19	[7]
Au/FeO_x	0.10	3.70	3.78	[7]
Au/Fe_2O_3	0.04	1.00	0.94	[8]
Au/α-Fe_2O_3 nanorods	0.05	0.50	4.00	[9]
Au/Fe_2O_3	0.004	2.50	4.68	[10]
Au/mesoporous Fe_2O_3	0.004	7.80	0.30	[11]
Au/CeO_2	0.10	5.70	0.005	[12]
Au/γ-Al_2O_3	0.15	0.17	0.022	[13]
Au/γ-Al_2O_3	n/a	1.00	1.62	[14]
Au/meso-TiO_2-450 film	n/a	27.8	0.37	[15]

All measurements were done at room temperature; WGC = World Gold Council

Notes for Table S2: The relatively small difference in the catalytic activity of the Au/Fe-MNF samples may be attributed to their nearly similar pore size distribution and pore volume as well as their surface area, with the difference being 63 m^2 g^{-1} at most. However, the optimum sample Au/Fe-MNF-350 exhibits better catalytic activity than the Au/Fe-MNF-400. This has been previously suggested to be caused by the higher redox property of Au/γ-Fe_2O_3 compared to Au/α-Fe_2O_3.[6] Furthermore, it has been reported that γ-Fe_2O_3 possesses cation vacancies which may adsorb metal to form stronger interaction with the deposited Au NPs and the oxygen species located in the vicinity of these cation vacancies is the most activated following exposure to CO, resulting in enhanced catalytic activity.[6] Based on these previous mechanistic studies, the active sites for the oxidation of CO at room temperature are proposed to be at the perimeter length of the Au/Fe_2O_3 interface as well as at the surface defects (*e.g.*, steps, edges, corners, and kinks) present on mesoporous Fe_2O_3 supports which have been regarded as active sites for the adsorption of reactants.[5, 16] Thus, during CO oxidation, oxygen is also adsorbed on these defect sites in addition to the deposited Au NPs and reacts with CO to produce CO_2. This in turn increases the reaction rate, leading to enhanced catalytic activity.

In the CO oxidation reaction, Au NPs serve to promote the adsorption of CO and they play a crucial role in activating the surface oxygen at the Au-Fe_2O_3 perimeter sites. Without Au NPs, surface oxygen of the Fe_2O_3 support is non-reactive under typical reaction conditions.[17] Furthermore, during CO oxidation, exposure of the Au/Fe_2O_3 catalysts to a CO/O_2 mixture promotes the generation of cationic Au ($Au^{\delta+}$) and metallic Au (Au^0).[18] Several studies have suggested that $Au^{\delta+}$ is the more active Au species for CO oxidation.[18, 19] The presence of active $Au^{\delta+}$ in the Au/Fe-MNF-350 (**Fig. S6d**) is expected to have enhanced its catalytic activity. As for the mesoporous Fe_2O_3 nanoflakes, they serve as excellent support materials to ensure uniform distribution of Au NPs and provide the cation vacancies which can promote stronger metal-support interactions.[6] Furthermore, the presence of hydroxyl (-OH) groups on the surface of the Fe_2O_3 support would promote the adsorption of CO at these -OH groups to form carbonate and more -OH groups *via* the deprotonation of bicarbonate and dissociation of H_2O.[16, 20]

References

1. Y. Yan, H. Tang, F. Wu, R. Wang and M. Pan, *Energies*, 2017, **10**, 1296.
2. Y. V. Kaneti, Q. M. D. Zakaria, Z. Zhang, C. Chen, J. Yue, M. Liu, X. Jiang and A. Yu, *J. Mater. Chem. A*, 2014, **2**, 13283-13292.
3. M. P. Casaletto, A. Longo, A. Martorana, A. Prestianni and A. M. Venezia, *Surf. Interface. Anal.*, 2006, **38**, 215-218.
4. A. A. Alshehri and K. Narasimharao, *J. Nanomater.*, 2017, **2017**, 14.
5. T. Akita, Y. Maeda and M. Kohyama, *J. Catal.*, 2015, **324**, 127-132.
6. K. Zhao, H. Tang, B. Qiao, L. Li and J. Wang, *ACS Catal.*, 2015, **5**, 3528-3539.
7. K. Zhao, B. Qiao, J. Wang, Y. Zhang and T. Zhang, *Chem. Commun.*, 2011, **47**, 1779-1781.
8. S. A. C. Carabineiro, N. Bogdanchikova, P. B. Tavares and J. L. Figueiredo, *RSC Adv.*, 2012, **2**, 2957-2965.
9. Z. Zhong, J. Ho, J. Teo, S. Shen and A. Gedanken, *Chem. Mater.*, 2007, **19**, 4776-4782.
10. K. Mikhail, C. G. Mool and D. Sarojini, *Nanotechnology*, 2004, **15**, 987.
11. S. Tanaka, J. Lin, Y. V. Kaneti, S.-i. Yusa, Y. Jikihara, T. Nakayama, M. B. Zakaria, A. A. Alshehri, J. You, M. S. A. Hossain and Y. Yamauchi, *Nanoscale*, 2018, **10**, 4779-4785.
12. S. Chen, L. Luo, Z. Jiang and W. Huang, *ACS Catal.*, 2015, **5**, 1653-1662.
13. S.-J. Lee and A. Gavriilidis, *J. Catal.*, 2002, **206**, 305-313.
14. Y.-F. Han, Z. Zhong, K. Ramesh, F. Chen and L. Chen, *J. Phys. Chem. C*, 2007, **111**, 3163-3170.
15. S. Akita, M. Amemiya, T. Matsumoto, Y. Jikihara, T. Nakayama, A. Hossain Md. Shahriar, K. Kani, D. Ishii, T. Islam Md, X. Jiang, A. Fatehmulla, A. Farooq Wazirzada, Y. Bando, V. Malgras and Y. Yamauchi, *Chem.-Asian J.*, 2017, **12**, 877-881.
16. L. Zeng, K. Li, H. Wang, H. Yu, X. Zhu, Y. Wei, P. Ning, C. Shi and Y. Luo, *J. Phys. Chem. C*, 2017, **121**, 12696-12710.
17. D. Widmann and R. J. Behm, *Angew. Chem. Int. Ed.*, 2011, **50**, 10241-10245.
18. S. Minicò, S. Scirè, C. Crisafulli, A. M. Visco and S. Galvagno, *Catal. Lett.*, 1997, **47**, 273-276.
19. G. J. Hutchings, M. S. Hall, A. F. Carley, P. Landon, B. E. Solsona, C. J. Kiely, A. Herzing, M. Makkee, J. A. Moulijn, A. Overweg, J. C. Fierro-Gonzalez, J. Guzman and B. C. Gates, *J. Catal.*, 2006, **242**, 71-81.
20. H.-Y. Lin and Y.-W. Chen, *Ind. Eng. Chem. Res.*, 2005, **44**, 4569-4576.